Envelope-function based transport simulation of a graphene ribbon with an antidot lattice

Paolo Marconcini, *Member, IEEE,* and Massimo Macucci

Abstract—We have performed numerical simulations to study the effect of a regular lattice of antidots on the conductance, and in particular on the gap, of an armchair graphene ribbon. We have used an envelope function approach, with a nonzero mass term mimicking the presence of the antidots. With a very efficient simulation procedure, consisting in a reciprocal space solution of the envelope function equation in the transverse direction followed by a recursive scattering matrix calculation in the transport direction, we have been able to analyze the impact of the different geometrical parameters characterizing the structure. We have observed that the conductance of the device rapidly reaches an asymptotic value when the length of the region containing the antidot lattice is increased. The dependence of the energy gap on the geometrical features of the antidot lattice is quite similar to that observed in unconfined graphene, excluding the cases of very small or distant antidots, when the energy gap of the pristine graphene ribbons is recovered. The tilt angle of the lattice with respect to the transport direction has a negligible influence on the gap, which is also quite robust with respect to the introduction of disorder in the antidot lattice.

Index Terms—graphene ribbons, antidot lattices, energy gap, transport calculation, Dirac equation

I. INTRODUCTION

Graphene, a two-dimensional honeycomb lattice of carbon atoms isolated by Geim and Novoselov in 2004 [1], represents one of the most studied materials of the last few years. It has been found that its low-energy transport behavior is governed by the same relations (the Dirac-Weyl equation [2], [3]) which define the relativistic behavior of massless spin-$1/2$ fermions and therefore exhibits quite exotic effects characteristic of relativistic quantum physics [4]. Moreover, it presents excellent material properties [5], [6], such as high mobility, mechanical strength, transparency, thermal conductivity, which are finding application in several industrial fields. Transistors based on graphene have been proposed, in order to exploit its high mobility and single-atom thickness to achieve high switching speed and excellent electrostatic control of the channel. While this material is very promising (and in some cases applications have already been found) for the implementation of sensors or radiofrequency transistors, up to now the use of graphene in digital electronics has been hindered by the fact that unconfined monolayer graphene is a zero gap material and this prevents the fabrication of devices with the large $I_{\mathrm{on}}/I_{\mathrm{off}}$ ratio (i.e. the ratio of the current in the on state to that in the off state) required by digital applications (at least of the

order of 10^4) [7]. Different methods have been proposed to generate a gap in graphene, among which lateral confinement, the introduction of an antidot lattice, doping, functionalization, the application of an orthogonal electric field over a bilayer graphene sheet.

In particular, if a graphene sheet is laterally confined (in this way obtaining a ribbon), a gap appears, with a value that on the average is inversely proportional to the width of the ribbon, but strongly depends (with a modulo 3 dependence) on the exact number of dimer lines inside the ribbon. Therefore, exact control of the gap would require atomistic precision in the lateral definition of the ribbon, which is unrealistic with current lithographic techniques.

Gap formation as a consequence of the introduction of an antidot lattice appears to be less sensitive to the achievable precision and several techniques have been exploited: e-beam lithography [8], diblock copolymer lithography [9], [10], nanosphere lithography [11], [12] and nanoimprint lithography [13], obtaining lattice periods of the order of tens or hundreds of nanometers.

Most of above mentioned experiments have been performed on graphene ribbons, rather than on extended graphene sheets, which is consistent with realistic device concepts. One can envisage channels obtained with lithographic processes, in analogy with what is currently done in silicon, which are then properly gated to obtain field effect transistors. In order to avoid extreme lithographic challenges and to mitigate the effect of edge roughness, the minimum conceivable ribbon width will be of a few tens of nanometers. If significant current carrying capabilities are needed, the ribbon width will be increased, probably up to a few hundred nanometers. These approaches do not guarantee atomic scale precision and, in particular, the exact nature of the edges, but encouraging results in terms of bandgap opening have been achieved, in particular in Refs. [12], [13]. It is in principle possible to achieve better control, in particular of the nature of the edges, using nanosculpting of graphene with a high-energy electron beam in a transmission electron microscope and successive annealing [14], although such an approach does not seem applicable for large-scale fabrication, at least in the near future.

Several theoretical studies have so far focused on the effect of antidot lattices on unconfined graphene [15]–[20].

Considering that most of the available experimental transport data on antidot lattices are for ribbons, we have decided to develop a numerical approach for the specific case of ribbons with a width between a few tens of nanometers and a few microns. For this size range atomistic methods become computationally very expensive, and therefore we have used an envelope function approach. In particular, we study the

P. Marconcini is with Dipartimento di Ingegneria dell'Informazione, Università di Pisa, Via Girolamo Caruso 16, 56122 Pisa, Italy p.marconcini@iet.unipi.it

M. Macucci is with Dipartimento di Ingegneria dell'Informazione, Università di Pisa, Via Girolamo Caruso 16, 56122 Pisa, Italy m.macucci@mercurio.iet.unipi.it

effect of an antidot lattice on a graphene armchair ribbon. In Section II we describe the numerical technique that we have developed, based on the solution of the envelope function equation (Dirac equation) in the reciprocal space and on the recursive scattering matrix approach for the determination of the transmission matrix of the device. Then, in Section III, we report the results that we have obtained with the application of this method to the study of the dependence of the conductance and of the energy gap on different geometrical parameters of the structure.

II. SIMULATION METHOD

For our calculations, we have chosen to adopt a continuum, envelope-function model for graphene, abandoning an exact atomistic description in favor of a much faster approach. To this purpose, we have generalized the envelope function based code that we have previously developed and applied to the study of devices based on monolayer graphene [21]–[23]. In transport simulations, the ribbon has been assumed as made up of many cascaded thin slices, chosen in such a way that within each slice both the geometry and the potential approximately do not vary in the transport direction (i.e., along x) but only in the transverse direction (i.e., along y), while the variations in the transport direction take place only at the interfaces between adjacent slices. The two-dimensional envelope-function equation has been separately solved in each slice, where it turns into a simpler one-dimensional differential problem. Then, the effect of the variation along the transport direction has been accounted for by enforcing the correct boundary conditions at the interfaces between adjacent slices and using a recursive scattering-matrix approach for the evaluation of the transmission matrix of the ribbon. An exact description of the edges of the antidots would have required a subdivision of the ribbon into a very large number of slices with a length of the order of the interatomic distance, in such a way as to take into account the atomistic changes of geometry of the ribbon with proper boundary conditions (following Ref. [23]). Since this would have severely decreased the code efficiency, we have chosen to approximate the presence of antidots by introducing into the envelope-function of graphene (i.e., the Dirac equation [2], the same relation which describes spin-1/2 particles in relativistic quantum mechanics) a space-varying term $m(\boldsymbol{r})v_F^2$ (where $m(\boldsymbol{r})$ is a mass which depends on the position $\boldsymbol{r}$, while v_F is the Fermi velocity of graphene) [15], [24]. As we show in Fig. 1, this fictitious mass term ("fictitious" because monolayer graphene is actually a zero-mass material) is taken as nonzero (and with a value much greater than the injection energy E of the carriers) only inside the antidots, where (exactly as in relativistic quantum mechanics) it locally introduces a large gap which, by keeping the carriers outside these regions, emulates the absence of carbon atoms [25], [26]. This is one of the possible approaches to the enforcement of energy independent hard-wall boundary conditions for the Dirac equation [27]. It has been previously shown [18] that this approximation can correctly reproduce the low-energy transport characteristics if the antidots do not present large zigzag edges (while it is not able to predict the presence of the localized edge states that propagate along this kind of edges).

Adopting an envelope function approximation, the graphene wave function can be expressed as [2]

$$\psi(\boldsymbol{r}) = \sum_{\boldsymbol{R}_A} \psi_A(\boldsymbol{R}_A)\varphi(\boldsymbol{r}-\boldsymbol{R}_A) + \sum_{\boldsymbol{R}_B} i\,\psi_B(\boldsymbol{R}_B)\varphi(\boldsymbol{r}-\boldsymbol{R}_B)\,,$$
(1)

where $\boldsymbol{R}_A$ and $\boldsymbol{R}_B$ represent the generic positions of the atoms of the two sublattices A and B of graphene and $\varphi(\boldsymbol{r})$ is the $2p^z$ orbital of the carbon atoms. The quantities $\psi_A(\boldsymbol{r})$ and $\psi_B(\boldsymbol{r})$, which modulate the atomic orbitals on the two sublattices, can be expressed in terms of the four envelope functions of graphene F_β^α (corresponding to the sublattices $\beta = A, B$ and to the Dirac points $\boldsymbol{\alpha} = \boldsymbol{K}, \boldsymbol{K'}$, with $\boldsymbol{K} = -K\hat{\boldsymbol{y}}$, $\boldsymbol{K'} = K\hat{\boldsymbol{y}}$, $K = 4\pi/(3a)$, and $a \approx 0.246$ nm the graphene lattice constant) as

$$\psi_\beta(\boldsymbol{r}) = e^{i\boldsymbol{K}\cdot\boldsymbol{r}}F_\beta^{\boldsymbol{K}}(\boldsymbol{r}) - i\,e^{i\boldsymbol{K'}\cdot\boldsymbol{r}}F_\beta^{\boldsymbol{K'}}(\boldsymbol{r})\,.$$
(2)

These envelope functions must satisfy the Dirac equation

$$[-i\gamma(\partial_x\sigma_x+\partial_y\sigma_y)+U(\boldsymbol{r})I+m(\boldsymbol{r})v_F^2\sigma_z]\boldsymbol{F}^{\boldsymbol{K}} = E\boldsymbol{F}^{\boldsymbol{K}}$$
$$[-i\gamma(\partial_x\sigma_x-\partial_y\sigma_y)+U(\boldsymbol{r})I+m(\boldsymbol{r})v_F^2\sigma_z]\boldsymbol{F}^{\boldsymbol{K'}} = E\boldsymbol{F}^{\boldsymbol{K'}}$$
(3)

where $\boldsymbol{F}^{\boldsymbol{\alpha}} = [F_A^{\boldsymbol{\alpha}}(\boldsymbol{r}), F_B^{\boldsymbol{\alpha}}(\boldsymbol{r})]^T$, $\gamma = v_F\hbar$ ($\hbar$ is the reduced Planck constant), $\partial_x = \partial/\partial x$, $\partial_y = \partial/\partial y$, σ_x, σ_y and σ_z are the Pauli matrices, $U(\boldsymbol{r})$ is the potential energy, and E is the injection energy.

As shown in Refs. [2], [28], Dirichlet boundary conditions have to be enforced on the wave function $\psi(\boldsymbol{r})$ at the "effective edges" of the ribbon, i.e. on the two lines of empty points of the graphene lattice (immediately under and over the ribbon) which are nearest neighbors of the carbon atoms at the actual edges of the ribbon but are not occupied by carbon atoms (see Fig. 1). In particular, in our simulations we consider armchair ribbons with effective edges at $y = 0$ and $y = \tilde{W}$ (the "effective width" of the ribbon). Since each of the two effective edges of an armchair ribbon contains A and B atoms, the Dirichlet boundary condition has to be enforced on $\psi_A(\boldsymbol{r})$ and $\psi_B(\boldsymbol{r})$ on both edges. In terms of the envelope functions, these boundary conditions can be expressed as

$$\boldsymbol{F}^{\boldsymbol{K}}(x, y=0) = i\boldsymbol{F}^{\boldsymbol{K'}}(x, y=0)$$
$$\boldsymbol{F}^{\boldsymbol{K}}(x, y=\tilde{W}) = ie^{i2K\tilde{W}}\boldsymbol{F}^{\boldsymbol{K'}}(x, y=\tilde{W})\,.$$
(4)

As previously mentioned, the ribbon is subdivided into cascaded slices in each of which both the potential energy and the mass term approximately do not depend on x. As a consequence of this invariance in the transport direction, in each of these slices the wave function and thus the envelope functions can be written as the product of a plane wave propagating in the x direction and of a transverse function depending only on y: $F_\beta^{\boldsymbol{\alpha}}(\boldsymbol{r}) = \Phi_\beta^{\boldsymbol{\alpha}}(y)e^{i\kappa_x x}$. Defining $\boldsymbol{\varphi}^{\boldsymbol{K}}(y) = [\Phi_A^{\boldsymbol{K}}(y), \Phi_B^{\boldsymbol{K}}(y)]^T$ and $\boldsymbol{\varphi}^{\boldsymbol{K'}}(y) = i[\Phi_A^{\boldsymbol{K'}}(y), \Phi_B^{\boldsymbol{K'}}(y)]^T$, the differential problem (3) with the boundary conditions (4) becomes:

$$(\sigma_z\partial_y + \sigma_x f(y) - i\sigma_y q(y))\,\boldsymbol{\varphi}^{\boldsymbol{K}}(y) = -\kappa_x\boldsymbol{\varphi}^{\boldsymbol{K}}(y)$$
$$(-\sigma_z\partial_y + \sigma_x f(y) - i\sigma_y q(y))\,\boldsymbol{\varphi}^{\boldsymbol{K'}}(y) = -\kappa_x\boldsymbol{\varphi}^{\boldsymbol{K'}}(y)$$
$$\boldsymbol{\varphi}^{\boldsymbol{K}}(0) = \boldsymbol{\varphi}^{\boldsymbol{K'}}(0)$$
$$\boldsymbol{\varphi}^{\boldsymbol{K}}(\tilde{W}) = e^{i2K\tilde{W}}\boldsymbol{\varphi}^{\boldsymbol{K'}}(\tilde{W})$$
(5)

where $f(y) = (U(y) - E)/\gamma$, $q(y) = m(y)v_F^2/\gamma$, and the quantity K, which appears only in the term $e^{i2K\tilde{W}}$, can be replaced by $\tilde{K} = K - n_0\pi/\tilde{W}$ with $n_0 = \text{round}\left(K\tilde{W}/\pi\right)$. This system of four differential equations with four boundary conditions on the domain $[0, \tilde{W}]$ can be transformed into an equivalent system of two differential equations with periodic boundary conditions on the domain $[0, 2\tilde{W}]$, defining the two-component function [21], [29]:

$$\varphi(y) = \begin{cases} e^{-i\tilde{K}y}\varphi^{K}(y) & y \in [0, \tilde{W}] \\ e^{i\tilde{K}(2\tilde{W}-y)}\varphi^{K'}(2\tilde{W} - y) & y \in [\tilde{W}, 2\tilde{W}]. \end{cases} \quad (6)$$

In terms of this new function, the boundary conditions in $y = 0$ of the original system (5) become periodic boundary conditions on the new domain $[0, 2\tilde{W}]$, while the boundary conditions in $y = \tilde{W}$ of Eq. (5) represent only continuity conditions in $y = \tilde{W}$. Therefore, the system (5) becomes

$$\left((\partial_y + i\tilde{K})\sigma_z + \tilde{f}(y)\sigma_x - i\,\tilde{q}(y)\sigma_y\right)\varphi(y) = -\kappa_x\varphi(y)$$

$$\varphi(2\tilde{W}) = \varphi(0) \quad (7)$$

with $\tilde{f}(y) = f(\tilde{W} - |\tilde{W} - y|)$ and $\tilde{q}(y) = q(\tilde{W} - |\tilde{W} - y|)$. This differential system with periodic boundary conditions can be efficiently solved in the reciprocal space (avoiding the fermion doubling problem which appears when a standard discretization technique in the direct space is applied to the solution of the Dirac equation [21]). Indeed, substituting the Fourier expansions of the known functions $\tilde{f}(y)$ and $\tilde{q}(y)$

$$\tilde{f}(y) = \sum_{m=-\infty}^{\infty} f_m e^{im\pi y/\tilde{W}}, \quad \tilde{q}(y) = \sum_{p=-\infty}^{\infty} q_p e^{ip\pi y/\tilde{W}} \quad (8)$$

and of the unknown function $\varphi(y)$

$$\varphi(y) = \sum_{\ell=-\infty}^{\infty} a_\ell e^{i\ell\pi y/\tilde{W}} \quad (9)$$

into the differential equations and projecting the resulting relations onto the set of basis functions $e^{in\pi y/\tilde{W}}$, a set of equations of the form:

$$\sum_{\ell=-\infty}^{+\infty}\left[\sigma_z\left(i\frac{n\pi}{\tilde{W}} + i\tilde{K}\right)\delta_{\ell,n} + \sigma_x f_{n-\ell} - i\sigma_y q_{n-\ell}\right]a_\ell = -\kappa_x a_\ell \quad (10)$$

is obtained, which represents an eigenproblem in the longitudinal wave vectors κ_x and in the Fourier coefficients a_ℓ of the functions $\varphi(y)$. After limiting its size with a proper cut-off of the Fourier components, this eigenproblem can be numerically solved, obtaining the envelope functions in each slice of the device. In particular, generalizing the result already observed in the absence of the mass term [21], it is possible to prove that if the longitudinal κ_x is an eigenvalue of the system, also $-\kappa_x$, κ_x^* and $-\kappa_x^*$ are possible eigenvalues ($Z_2 \times Z_2$ symmetry). As an example, in Fig. 2 we show the values of κ_x that we have obtained for $E = 0.1$ eV in a slice with 4878 dimer lines, when the mass term $m(y)v_F^2$ in the slice has the profile shown in the inset and the potential $U(y)$ is identically null (as in all the simulations that we will show in the following).

For each solution of the linear system, i.e. for each mode of the slice, the A and B components of the wavefunction can
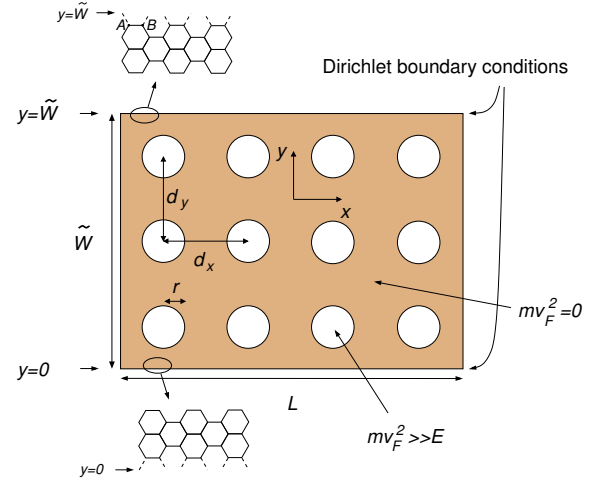

Fig. 1. Sketch of the ribbon with a square (rectangular in general) lattice of circular antidots. Here we show the different geometrical parameters and the assumptions and boundary conditions that we have used in the simulations.
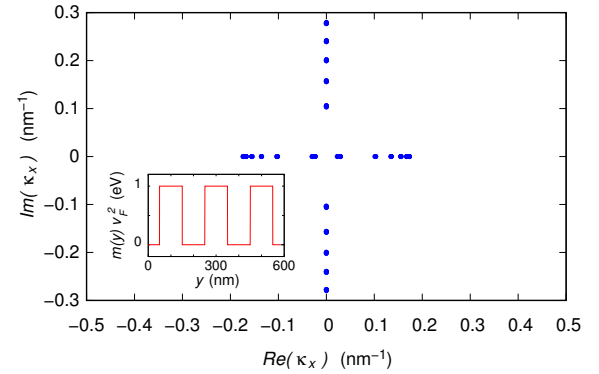

Fig. 2. Values of the longitudinal wave vector κ_x that are obtained for $E = 0.1$ eV in a slice with 4878 dimer lines where the mass term $m(y)v_F^2$ has the profile shown in the inset and the potential $U(y)$ is identically null.

be expressed in this way (exploiting the relations (2), (6) and (9)):

$$\psi_\beta(x, y) = 2i\sum_\mu\left\{[a^\beta]_\mu \sin[(\mu - n_0)\pi y/\tilde{W}]\right\}e^{i\kappa_x x}. \quad (11)$$

Following this analytical procedure, we have computed the transport modes in each of the slices into which the ribbon has been divided. Then, we have obtained the scattering matrices which couple the modes in adjacent slices using the mode-matching technique described in Ref. [21]. For each couple of slices, we have proceeded in the following way. Imagining to inject one mode at a time, when this mode impinges against the interface between the two slices (which represents the discontinuity) it gives rise to a number of reflected modes and of transmitted modes. We have enforced the continuity of $\psi_A(r)$ and $\psi_B(r)$ at the interface. The wavefunction can be written, on one side of the interface, as the sum of the injected mode and of the reflected modes multiplied by the reflection coefficients, and, on the other side, as the sum of the transmitted modes multiplied by the transmission coefficients. Writing the continuity equations for all the possible modes that can be injected into the pair of

slices (i.e. for all the modes that we have computed in the two slices) and projecting these relations onto a basis consisting of sine functions $\sin((j - n_0)\pi y/\tilde{W})$, we have obtained a linear system in the reflection and transmission coefficients, i.e. in the elements of the scattering matrix. This calculation has been performed directly in terms of the Fourier coefficients of the function $\varphi(y)$, without the necessity to anti-transform them. Then, the series of scattering matrices connecting pairs of slices of the ribbon has been recursively composed following a standard procedure [30], obtaining the scattering matrix and, in particular, the transmission matrix t of the ribbon. Finally, from this quantity we have computed the conductance G using the Landauer-Büttiker approach [31]:

$$G = \frac{2\,q^2}{h} \sum_i w_i \,, \qquad (12)$$

where q is the elementary charge, h is Planck's constant, and the w_i's are the eigenvalues of the matrix $t^\dagger t$. From the transmission matrix t, also the shot noise power spectral density S_I and the Fano factor η (i.e., the ratio between S_I and the full shot noise power spectral density expected from Schottky's theorem $2q|I|$, where I is the average current flowing through the ribbon when a voltage V is applied) have been computed using these expressions [32]:

$$S_I = 4\,\frac{q^3}{h}\,|V| \sum_i w_i\,(1 - w_i)\,, \ \ \eta = \frac{\sum_i w_i(1 - w_i)}{\sum_j w_j} \,. \quad (13)$$

In all the calculations, we had to consider quite a large number of modes, in such a way as to properly simulate the behavior of the wave function in the slices where the antidots subdivide the ribbon into several totally decoupled transport channels.

III. NUMERICAL RESULTS

In our simulations we have considered armchair ribbons with circular holes (with radius r), modeled with regions where the term mv_F^2 is nonzero and much greater than the injection energy E (see Fig. 1). More in detail, in all the simulations that we report here we have taken the term mv_F^2 equal to 1 eV (or 10 eV, in the cases in which we had to consider a larger range of injection energies). The potential energy U has been assumed as zero all over the ribbon. Most simulations have been performed on a regular rectangular lattice of antidots (even though, as we will detail in the following, also different lattices have been examined). For rectangular lattices, we have defined as d_x and d_y the distances between the centers of nearest neighbor holes in the transport and transverse direction, respectively. In the particular case of square lattices, $d_x = d_y = d$, as shown in Fig. 1.

It has been shown in the literature that the introduction of a regular array of antidots into unconfined graphene gives rise to an energy gap. In our simulations, we have estimated the energy gap E_g from the behavior of the conductance G as a function of the energy E of the carriers, considering E_g as the width of the energy interval, near $E = 0$, where G is less than a given threshold, that we have taken as $0.02\,G_0$ (where $G_0 = 2\,q^2/h$ is the conductance quantum).
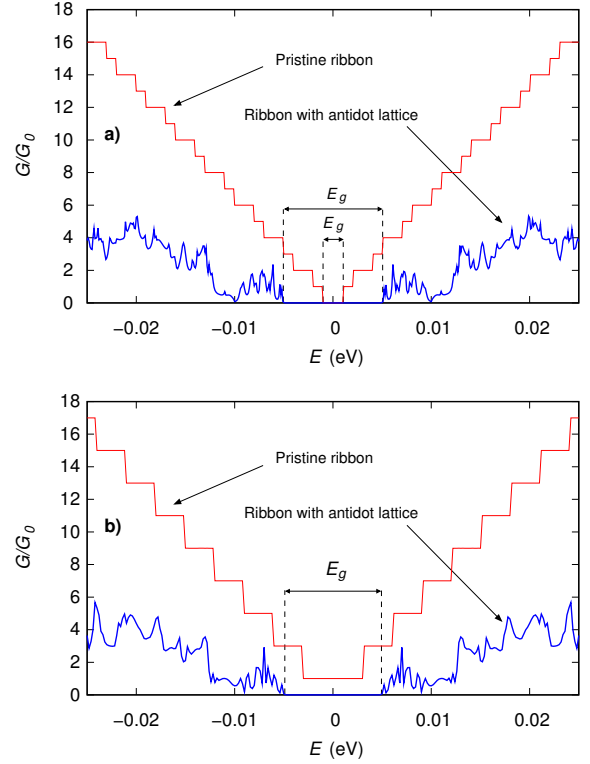

Fig. 3. Conductance G (normalized with respect to the conductance quantum $G_0 = 2\,q^2/h$) as a function of the energy E of the carriers in two 600 nm wide and 800 nm long armchair ribbons with a regular square lattice of circular antidots with $r = 50$ nm and $d = 200$ nm. The two ribbons differ for the exact number of dimer lines: 4878 in (a) and 4877 in (b).

In order to investigate the effect of the antidot lattice on a confined structure, we have first considered two 600 nm wide and 800 nm long armchair ribbons with a regular square lattice of circular antidots with $r = 50$ nm and $d = 200$ nm (Fig. 1). The two ribbons differ for the exact number of dimer lines across their width: 4878 in the first case (corresponding to a semiconducting ribbon with energy gap $E_g = 2\gamma\pi/(3\tilde{W}) \simeq 2$ meV) and 4877 in the second case (corresponding to a metallic ribbon with null energy gap). As we show in Fig. 3, in the presence of the antidot lattice the conductance strongly decreases with respect to that in the pristine structures and in particular both ribbons exhibit a gap of about 10 meV. Therefore, the antidot lattice has the effect of enlarging the energy gap in semiconducting ribbons, and to make it appear in ribbons that would otherwise be metallic.

In Fig. 4, we represent the conductance as a function of the energy of the carriers over a larger energy range for the ribbon with 4878 dimer lines with a different square lattice of circular antidots (shown in the inset), characterized by $r = 15$ nm and $d = 100$ nm. With respect to the pristine graphene ribbon, we observe a more irregular behavior, with a partial formation, around the gap, of minibands, which are introduced by the regular lattice of antidots.

We have performed a wide range analysis of the dependence of the conductance behavior, and in particular of the energy gap, on the different geometrical parameters which characterize the structure.
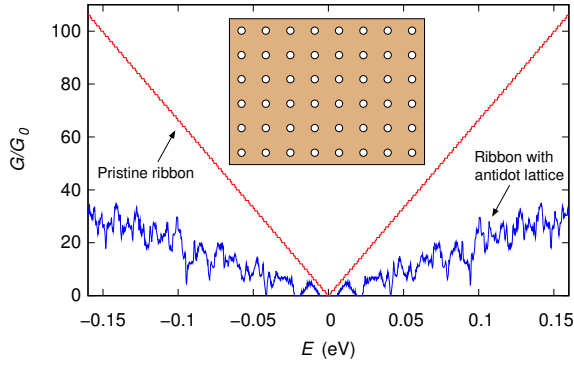
Fig. 4. Behavior of the conductance G as a function of the energy E in the 600 nm wide and 800 nm long armchair ribbon (with 4878 dimer lines) sketched in the inset, with a regular square lattice of circular antidots characterized by $r = 15$ nm and $d = 100$ nm.

We have first considered a ribbon with an antidot lattice of finite extension along the transport direction x, and we have studied the dependence of its conductance on the length of the antidot region. In particular, we have simulated an armchair ribbon with 4878 dimer lines across its width and we have progressively increased the number of columns of antidots. We have taken circular antidots with radius $r = 25$ nm, located on a square lattice with a period $d = 100$ nm (inset of Fig. 5(a)). As we show in Fig. 5(a), where we report the results obtained for an injection energy $E = 0.1$ eV, for this particular geometry (with $d = 4r$) the conductance in the presence of a single column of antidots is about one half of that of the pristine ribbon, since in the presence of the perforations only half of the ribbon width is available for charge transport. Further increasing the number of antidot columns, and thus the length of the antidot region, the conductance continues to decrease. However, above a certain number of columns (about 5-6 in the case reported) an asymptotic value, characteristic of the case in which the antidot lattice extends all over the ribbon, is reached. In Fig. 5(b) we show that a similar behavior is observed for the value E_g of the gap, estimated from the behavior of G as a function of E: E_g increases with the number of antidot columns, until it reaches an asymptotic value characteristic of the periodically perforated ribbon.

Then we have computed the conductance of a 600 nm wide armchair ribbon (containing 4878 dimer lines) with a square lattice of circular antidots for different values of the antidot radius r and of the distance d between the antidots, for an injection energy $E = 0.1$ eV. In Fig. 6(a) we report the behavior of the conductance for a lattice with $d = 100$ nm, as a function of the radius of the antidots: as one could expect, starting from the value of the pristine ribbon (when $r = 0$), G progressively decreases and vanishes when the channels between the antidots are so narrow that no mode is able to propagate through them. In Fig. 6(b) we show the dual dependence of G on the period d of the square lattice for a fixed value of the antidot radius $r = 15$ nm: starting from zero for a value of d for which the antidots coalesce, G increases towards the value characteristic of the unperforated ribbon.

In Fig. 7 we show the behavior of the Fano factor η as a function of the energy E of the carriers for the same
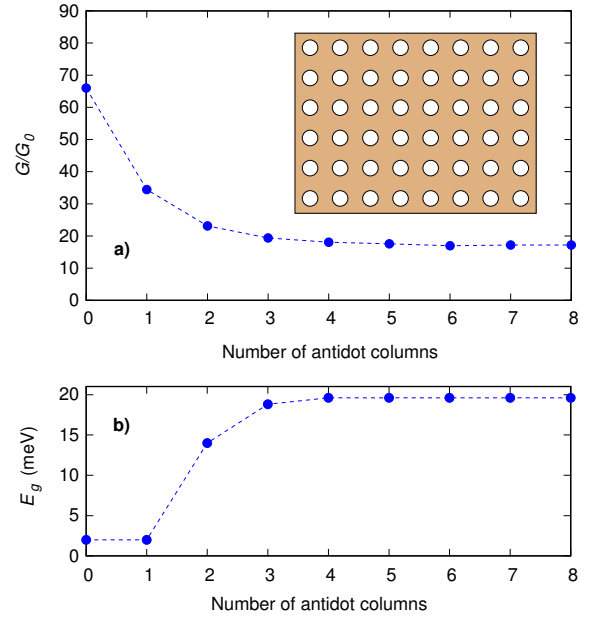

Fig. 5. Normalized conductance (for $E = 0.1$ eV) of a 600 nm wide and 800 nm long armchair ribbon in the presence of a square lattice of circular antidots with $r = 25$ nm and $d = 100$ nm (inset of panel (a)), as a function of the number of antidot columns (and thus of the length of the antidot region). In panel (b) we report the corresponding value of E_g, estimated from the behavior of G as a function of E.
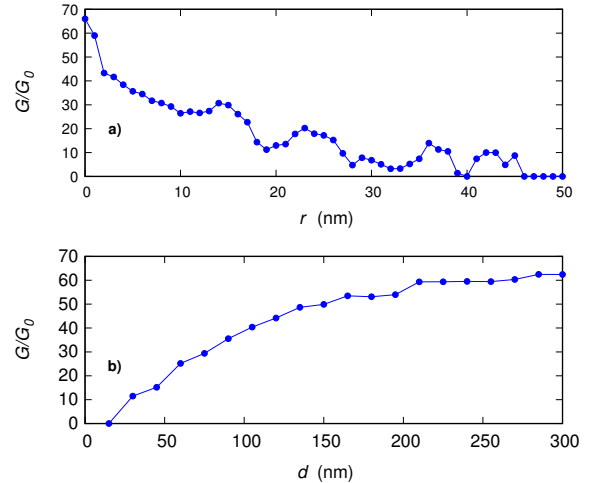

Fig. 6. Normalized conductance of a 600 nm wide and 800 nm long armchair ribbon with a square lattice of circular antidots, computed: a) as a function of the antidot radius r for a fixed distance $d = 100$ nm between the antidots, and b) as a function of d when r is kept constant at 15 nm. In both cases, the energy E is 0.1 eV.

ribbon with 4878 dimer lines and a square antidot lattice with $d = 100$ nm, for four values of the antidot radius: 5 nm, 15 nm, 25 nm and 35 nm. Increasing the energy E, the fluctuations decrease (because they average over a greater number of propagating modes) and the Fano factor settles around a value that increases enlarging the antidot size. Actually, enlarging the antidots the probability for the carriers to be transmitted through the ribbon decreases and the correlations between the carriers which determine the shot noise suppression decrease, too.
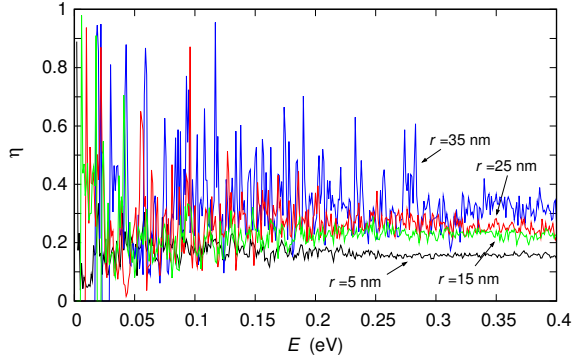
Fig. 7. Fano factor as a function of the energy E, computed for a 600 nm wide and 800 nm long armchair ribbon with a square lattice of circular antidots with $d = 100$ nm, for four values of the antidot radius r.
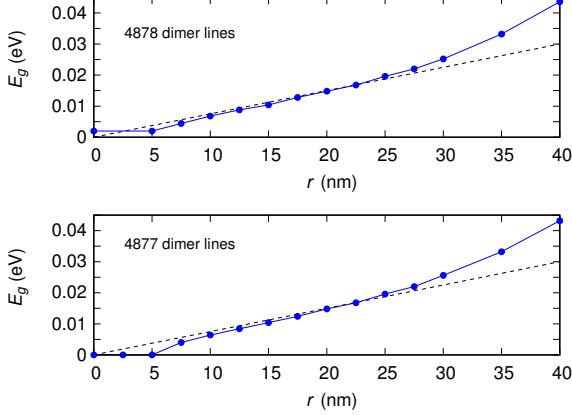

Fig. 8. Behavior of the energy gap as a function of the antidot radius for two armchair ribbons (containing 4878 and 4877 dimer lines, respectively) with a square lattice of antidots with $d = 100$ nm. The dashed curves represent an analytical fit with the relation (14).
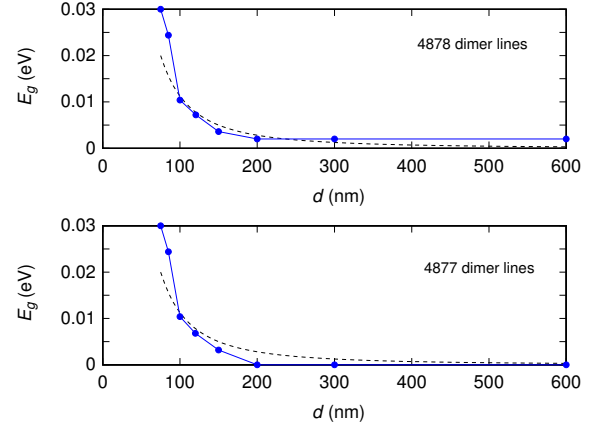

Fig. 9. Behavior of the energy gap as a function of the distance d between the antidots for two armchair ribbons (containing 4878 and 4877 dimer lines, respectively) with a square lattice of antidots with $r = 15$ nm. The dashed curves represent an analytical fit with the relation (14).
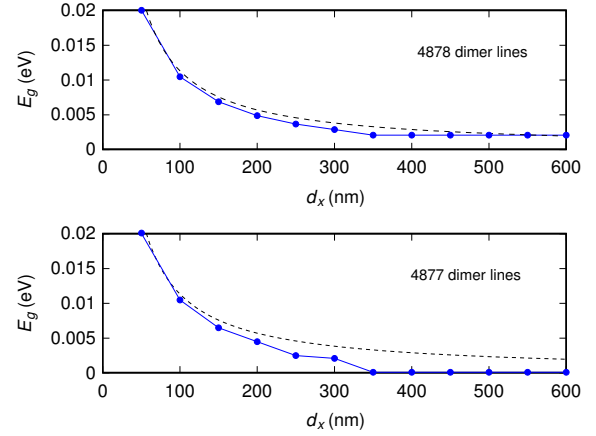

Fig. 10. Behavior of the energy gap as a function of the distance d_x for two armchair ribbons (containing 4878 and 4877 dimer lines, respectively) with a rectangular lattice of antidots with $r = 15$ nm and $d_y = 100$ nm. The dashed curves represent an analytical fit with the relation (14).

We have then studied the dependence of the energy gap E_g on the radius r of the antidots and on the distance d between the antidots in the two 600 nm wide armchair ribbons that we have previously taken into consideration, with 4878 and 4877 dimer lines (and thus characterized by a semiconducting and metallic behavior in the absence of antidots), respectively.

We have first considered the effect of a square antidot lattice.

In Fig. 8 we report the behavior of the energy gap in the ribbons with 4878 and 4877 dimer lines, respectively, as a function of the antidot radius for a fixed distance between the antidots $d = 100$ nm. Starting (for $r = 0$) from the value characteristic of the pristine ribbon (i.e., from 2 meV for the first ribbon and from 0 eV for the second one), for larger holes the gap increases about linearly with the radius.

We have also performed other simulations keeping the radius of the antidots constant at the value $r = 15$ nm and varying the period d of the square lattice. As shown in Fig. 9 for the two ribbons, we have found that the energy gap strongly decreases when the distance between the antidots increases, until it saturates at the value characteristic of the pristine ribbon (2 meV and 0 eV in the two cases).

We have then considered the effect on the energy gap of rectangular antidot lattices with a different distance between the antidots along the transport and transverse directions, i.e. with $d_x \neq d_y$. In Fig. 10 we report the results obtained in the two slightly different ribbons keeping d_y constant at 100 nm and varying d_x, while in Fig. 11 we show the results achieved by keeping $d_x = 100$ nm and varying d_y. In both cases the radius of the antidots is fixed at $r = 15$ nm. The behavior we have observed is quite similar, with an energy gap that decreases while increasing the distance, and saturating to the value characteristic of the pristine ribbons.

According to Refs. [15], [18], the introduction of a regular lattice of antidots in unconfined graphene gives rise to an energy gap

$$E_g \approx C\sqrt{N_{\mathrm{rem}}}/N_{\mathrm{tot}} = C'\sqrt{S_{\mathrm{antidot}}}/S_{\mathrm{unit\ cell}}. \quad (14)$$

If we define $\mathcal{A}$ the generical unit cell of the antidot lattice, N_{tot} is the total number of carbon atoms in the region $\mathcal{A}$ of the pristine ribbon, while N_{rem} is the number of carbon atoms that have been removed from this region in order to create the antidot. The quantities S_{antidot} and $S_{\mathrm{unit\ cell}}$ represent the areas of the antidot and of the unit cell $\mathcal{A}$, respectively.
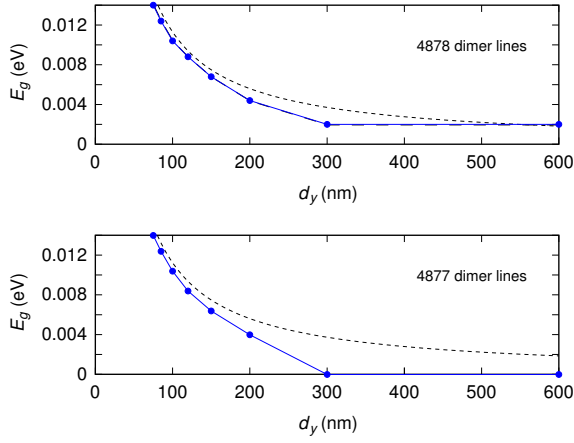
Fig. 11. Behavior of the energy gap as a function of the distance d_y for two armchair ribbons (containing 4878 and 4877 dimer lines, respectively) with a rectangular lattice of antidots with $r = 15$ nm and $d_x = 100$ nm. The dashed curves represent an analytical fit with the relation (14).

Finally, C and $C' = C/\sqrt{c}$ are proportionality constants of the order of 28.3 eV [18] and 4.58 eV·nm, respectively (where $c = 4/(a^2\sqrt{3}) \approx 38.177$ nm^{-2} is the concentration of carbon atoms in graphene). In the case of a rectangular lattice of circular antidots, $S_{\text{antidot}} = \pi r^2$, while $S_{\text{unit cell}} = d_x d_y$, and thus the energy gap E_g should be proportional to $r/(d_x d_y)$.

We have compared our results, achieved in the case of armchair ribbons, with this relation, obtained for the case of unconfined graphene. In Figs. 8-11 we have represented with dashed lines the curves given by the relation (14) with the values $C = 26.145$ eV and $C' = 4.2314$ eV·nm which best fit our numerical data. We observe that in the considered ribbons the dependence of the energy gap on the different geometrical parameters is similar to what has been previously obtained for unconfined graphene and approximately still follows the relation (14). For example, starting from the values $r = 15$ nm, $d_x = d_y = 100$ nm, we have verified that doubling at the same time r and d_x while keeping d_y constant (or vice versa), or increasing by a factor 4 the radius, while doubling both d_x and d_y, does not significantly alter the band gap of the ribbon, which remains of the order of 10 meV. The main differences with respect to the relation (14) appear when the distance between the antidots is comparable with the size of the ribbon, since in those cases the ribbon contains only a limited number of isolated antidots and thus (being the effect on the gap of the antidot lattice inhibited by the limited size of the ribbon) the gap is mainly determined by the confinement of the ribbon. Analogously, when the antidots have a very small radius and thus the effect of the antidot lattice on the gap would be very limited also in unconfined graphene, the energy gap is mainly determined by the lateral confinement of the ribbon. In Fig. 12 we show the behavior of the energy gap as a function of the antidot radius when a square antidot lattice with period $d = 100$ nm is introduced in armchair semiconducting ribbons with several widths: 200 nm, 300 nm, and 600 nm. We observe again that for small values of the antidot radius, the value of the energy gap is determined only by the ribbon width, i.e. by the quantization of the transverse
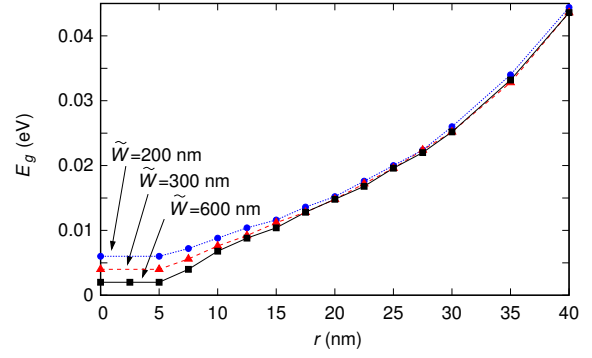

Fig. 12. Behavior of the energy gap as a function of the antidot radius for three semiconducting armchair ribbons with width equal to 200 nm, 300 nm, and 600 nm, in the presence of a square lattice of antidots with $d = 100$ nm.
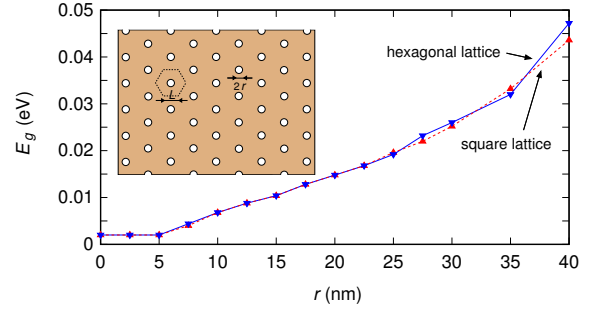

Fig. 13. Behavior of the energy gap as a function of the antidot radius for an armchair ribbon with 4878 dimer lines in the presence of a hexagonal lattice of antidots (sketched in the inset) with the edge of the unit cell kept constant at the value $L = 62.04$ nm, compared with the behavior already observed in the case of a square lattice with $d = 100$ nm.

wave vector deriving from the Dirichlet boundary conditions at the effective edges of the ribbon.

In order to perform a further test of this dependence, we have made some simulations also for a hexagonal lattice of circular antidots (see the inset of Fig. 13). While for a square lattice with period d the area of the unit cell is $S_{\text{unit cell}} = d^2$, for this hexagonal lattice, if we define as L the edge of the hexagonal unit cell $S_{\text{unit cell}} = \sqrt{3}L^2 3/2$. If the relation (14) is valid, a similar value of E_g should be obtained in the presence of a square lattice with period d and of an hexagonal lattice with $L = d\sqrt{2/(3\sqrt{3})}$. In Fig. 13 we report, for the armchair ribbon with 4878 dimer lines in the presence of a hexagonal lattice, the behavior of the energy gap E_g as a function of the antidot radius r, if the the edge of the unit cell is kept constant at the value $L = 62.04$ nm (in such a way that the unit cell has the same area as that of the square lattice with $d = 100$ nm that we have previously considered). For comparison, we report also the behavior of E_g as a function of r that we have obtained with a square lattice with $d = 100$ nm (and that we already shown in Fig. 8(a)). We see that the behavior of E_g as a function of r is similar in the two cases.

In Fig. 14, instead, we report the results obtained for the ribbon with 4878 dimer lines with the hexagonal lattice keeping the antidot radius constant at $r = 15$ nm and varying the edge L of the hexagonal unit cell. On the horizontal axis we report, instead of L, the quantity $L\sqrt{(3\sqrt{3})/2}$, which
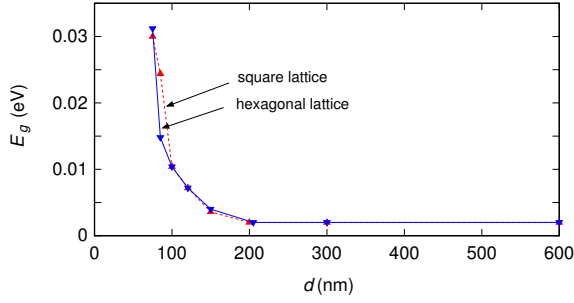
Fig. 14. Behavior of the energy gap as a function of d for an armchair ribbon with 4878 dimer lines in the presence of a hexagonal lattice of circular antidots with radius $r = 15$ nm, compared with the behavior already observed in the case of a square lattice with $r = 15$ nm. The quantity d, which in the case of the square lattice represents the lattice period, in the case of the hexagonal lattice is defined as $d = L\sqrt{(3\sqrt{3})/2}$ and represents the edge of a square cell which has the same area as the hexagon cell with edge L that we are considering.

corresponds to the period d of the square lattice with the same unit cell area as the hexagonal lattice, in such a way as to make the comparison with the data shown in Fig. 9(a) (replotted here) easier. We see that also this time the behavior is quite similar in the two cases and thus this dependence of E_g on the different geometrical parameters of the antidot lattice is quite general.

In conclusion, the dependence of the energy gap on the geometrical parameters of the antidot lattice is similar to what has been previously observed in unconfined graphene, except for the cases of distances between the antidots comparable with the ribbon size and of very small antidots: in both cases the effect of the antidot lattice actually vanishes and the lateral confinement of the ribbon tends to prevail.

As a consequence of the relation (14), i.e. of the fact that $E_g \approx C(\sqrt{N_{\text{rem}}/N_{\text{tot}}})(1/\sqrt{N_{\text{tot}}})$, for each fraction $N_{\text{rem}}/N_{\text{tot}}$ of removed atoms the energy gap can be increased reducing N_{tot}, i.e. the size of the unit cell of the antidot lattice. This means that high values of E_g could be obtained if we were able to fabricate a very dense periodic repetition of holes in the ribbon (with the present fabrication techniques, distances between the antidots of the order of tens of nanometers have been achieved). For example, in Fig. 15 we report the behavior of the conductance as a function of the energy that we have obtained for a 100 nm wide (with 813 dimer lines) and 200 nm long ribbon with and without a square lattice of circular antidots with $r = 1.5$ nm and $d = 7$ nm. While the pristine ribbon has a gap $E_g = 2\gamma\pi/(3\tilde{W}) \simeq 12$ meV, in the presence of the antidot lattice we obtain a quite large energy gap: $E_g \approx 0.36$ eV. In the inset we show the dependence of the energy gap on the antidot radius if the distance between the antidots is kept constant at $d = 7$ nm.

The same conclusion is valid also for lattices with a different geometry; for example introducing, into the 100 nm wide and 200 nm long ribbon, a hexagonal lattice of circular antidots with $L = 10a = 2.46$ nm and $r = 6.4a = 1.5744$ nm, we have obtained an energy gap $E_g \approx 1.15$ eV (i.e. a value of the order of the energy gap reported in the Table 1 of Ref. [15] for the case of unconfined graphene).
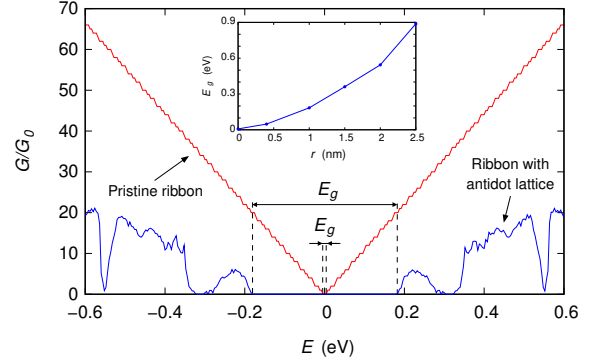

Fig. 15. Behavior of the conductance as a function of the energy E for a 100 nm wide (with 813 dimer lines) and 200 nm long ribbon with and without a square lattice of circular antidots with $r = 1.5$ nm and $d = 7$ nm. In the inset we report the dependence of the energy gap on r if d is kept constant at 7 nm.
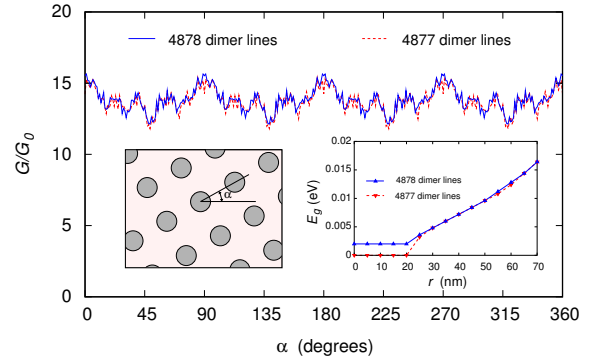

Fig. 16. Conductance of the two armchair ribbons with 4878 and 4877 dimer lines in the presence of a square antidot lattice with $d = 200$ nm and $r = 50$ nm, tilted by an angle α with respect to the transport direction x (see the left inset), as a function of α. The solid and dashed curve correspond to the ribbons with 4878 and 4877 dimer lines, respectively. In the right inset we show the dependence on the antidot radius r of the energy gap E_g of the two ribbons with a square antidot lattice with $d = 200$ nm.

We have then studied the dependence of the conductance and of the energy gap of a graphene ribbon with a square antidot lattice on the orientation α of the lattice with respect to the transport direction x (see the left inset of Fig. 16). We have simulated 600 nm wide and 800 nm long ribbons with a square lattice of antidots with $d = 200$ nm and $r = 50$ nm for different values of the tilt angle α. As we can see in the right inset of Fig. 16 (where we show the dependence of the energy gap on the antidot radius for the two armchair ribbons with 4878 and 4877 dimer lines with a square lattice of antidots with $d = 200$ nm) for $r = 50$ nm the gap of these ribbons is mainly determined by the effect of the antidot lattice. In Fig. 16 we report the conductance that we have obtained for $E = 0.1$ eV as a function of α, for the ribbons with 4878 and 4877 dimer lines. The two curves are nearly identical and in both cases the dependence on the orientation is very small.

Analogous conclusions can be drawn for the energy gap: in Fig. 17 we show the behavior of the energy gap E_g as a function of the tilt angle α for the two ribbons. Also in this case, the two lines are nearly superimposed and E_g does not show a significant dependence on α.

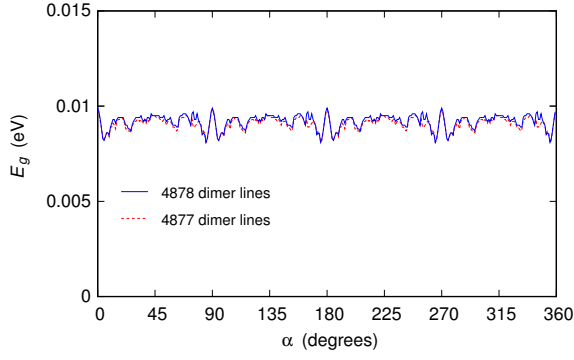This should be even more valid for a radius value such as

Fig. 17. Behavior of the energy gap of the two armchair ribbons with 4878 and 4877 dimer lines in the presence of a square antidot lattice with $d = 200$ nm and $r = 50$ nm, tilted by an angle α with respect to the transport direction x, reported as a function of α.

$r = 10$ nm for which, as we see in the right inset of Fig. 16, the energy gap depends mainly on the ribbon confinement, rather than on the presence of the antidots. Indeed, repeating the same simulations for $d = 200$ nm and $r = 10$ nm, in the two ribbons with 4878 and 4877 dimer lines we have found an energy gap of 2 meV and 0 eV, respectively (the values characteristic of the pristine ribbons), independent of the tilt angle. Also the value of the conductance does not exhibit any substantial dependence on α.

We conclude that in the structures we are considering, which do not include large zigzag edges at the borders of the ribbon and of the antidots, the energy gap does not depend on the orientation of the antidot lattice.

Finally, we have considered the effect on the gap of the presence of disorder in the antidot lattice, which will inevitably appear in the actual fabrication process. We have separately considered the effect of irregularities in the positions and in the size of the antidots.

We have performed our simulations on a 600 nm wide (with 4878 dimer lines) and 800 nm long ribbon, in the presence of an ideally square lattice of circular antidots with $d = 100$ nm and $r = 15$ nm. We have first introduced disorder in the positions of the antidots, adding to the original coordinates of the antidot centers random quantities uniformly distributed in the range $[-\Delta, \Delta]$ for several values of Δ, ranging from 0 to 20 nm, while keeping the radius of the antidots constant. In Fig. 18 we report the values of the conductance obtained as a function of the energy E of the carriers for three different values of Δ. We have considered only a single disorder realization for each value of Δ (in the inset of Fig. 18 we show the disorder realization considered for $\Delta = 20$ nm).

We have then performed a second set of simulations, keeping the position of the antidots constant while varying their radius: for each antidot we have summed to the original value of the radius $r = 15$ nm a random quantity uniformly distributed between $-\Delta r$ and Δr, with Δr between 0 and 7 nm. In Fig. 19 we report the value of G as a function of E for three different values of Δr. Also in this case, only one disorder realization has been simulated for each value of Δr (in the inset of Fig. 19 we show the disorder realization considered for $\Delta r = 7$ nm).
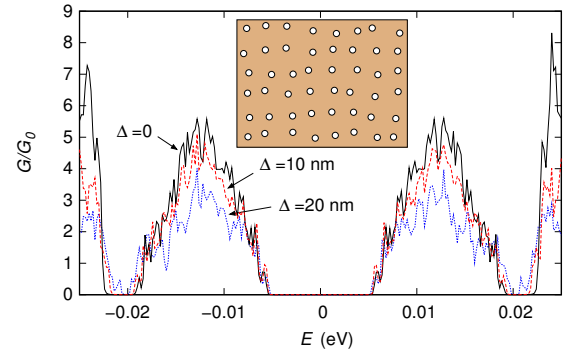

Fig. 18. Conductance of a 600 nm wide (with 4878 dimer lines) and 800 nm long ribbon in the presence of a square lattice of circular antidots with $d = 100$ nm and $r = 15$ nm with a disorder in the position of the antidots. Three different degrees of position disorder have been considered, with maximum displacement Δ (along x and y) from the ideal positions equal to 0 (no disorder), 10 nm, and 20 nm. In the inset we show a disorder realization with $\Delta = 20$ nm.
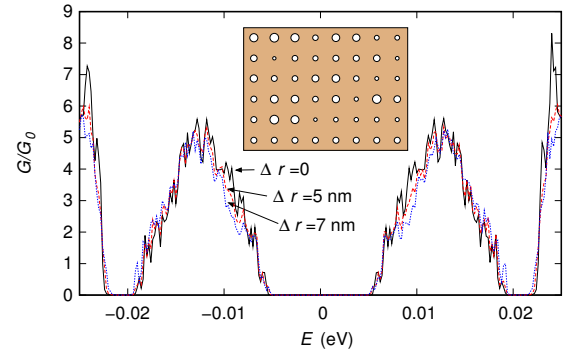

Fig. 19. Conductance of a 600 nm wide (with 4878 dimer lines) and 800 nm long ribbon in the presence of a square lattice of circular antidots with $d = 100$ nm and $r = 15$ nm with a disorder in the size of the antidots. Three different degrees of size disorder have been considered, with maximum deviation Δr of the antidot radius from the value $r = 15$ nm equal to 0 (no disorder), 5 nm, and 7 nm. In the inset we show a disorder realization with $\Delta r = 7$ nm.

From these results, the gap estimated from $G(E)$ seems rather robust to the presence of disorder, both in the position and in the size of the antidots. However, we must consider that, as we have done throughout the paper, the gap has been estimated from the behavior of the conductance as a function of the energy E and thus in this case includes, beyond the properly defined energy gap (the forbidden range of energy between the valence and the conduction bands), the suppression of conductance deriving from the breaking of the lattice periodicity and from the resulting Anderson localization [33]. Interestingly, in previous studies of unconfined graphene [34] it has been shown that these two forms of gap have a similar dependence on the geometrical parameters of the antidot lattice.

IV. CONCLUSION

Using an efficient simulation code based on the solution of the Dirac equation in the reciprocal space and on a recursive scattering matrix approach to transport calculation, we have analyzed the dependence of the conductance and of the energy gap of a graphene armchair ribbon with a regular lattice of

perforations on the different geometrical parameters characterizing the structure: the length of the antidot region, the radius of the antidots and their reciprocal distance, the width of the ribbon. We have found that introduction of an antidot lattice into a graphene ribbon can effectively give rise to a rather large energy gap, nearly insensitive to the tilt angle of the lattice and robust with respect to disorder, if we are able to fabricate a lattice with a sufficiently short repetition period. On the other hand, the presence of the antidots strongly suppresses the conductance of the ribbon and thus has a negative impact on the current flowing through the device.

REFERENCES

[1] K. S. Novoselov, A. K. Geim, S. V. Morozov, D. Jiang, Y. Zhang, S. V. Dubonos, I. V. Grigorieva, A. A. Firsov, "Electric Field Effect in Atomically Thin Carbon Films," *Science*, vol. 306, p. 666, 2004.

[2] P. Marconcini, M. Macucci, "The k·p method and its application to graphene, carbon nanotubes and graphene nanoribbons: the Dirac equation," *La Rivista del Nuovo Cimento*, vol. 34, no. 8-9, p. 489, 2011.

[3] A. H. Castro Neto, F. Guinea, N. M. R. Peres, K. S. Novoselov, A. K. Geim, "The electronic properties of graphene," *Rev. Mod. Phys.*, vol. 81, p. 109, 2009.

[4] M. I. Katsnelson, K. S. Novoselov, "Graphene: New bridge between condensed matter physics and quantum electrodynamics," *Solid State Commun.*, vol. 143, p. 3, 2007.

[5] A. K. Geim, K. S. Novoselov, "The rise of graphene," *Nat. Mater.*, vol. 6, p. 183, 2007.

[6] A. K. Geim, "Graphene: Status and Prospects," *Science*, vol. 324, p. 1530, 2009.

[7] F. Schwierz, "Graphene transistors," *Nat. Nanotech.*, vol. 5, p. 487, 2010.

[8] L. Z. Liu, S. B. Tian, Y. Z. Long, W. X. Li, H. F. Yang, J. J. Li, C. Z. Gu, "Tunable periodic graphene antidot lattices fabricated by e-beam lithography and oxygen ion etching," *Vacuum*, vol. 105, p. 21, 2014.

[9] M. Kim, N. S. Safron, E. Han, M. S. Arnold, P. Gopalan, "Fabrication and Characterization of Large-Area, Semiconducting Nanoperforated Graphene Materials," *Nano Lett.*, vol. 10, p. 1125, 2010.

[10] J. Bai, X. Zhong, S. Jiang, Y. Huang, X. Duan, "Graphene nanomesh," *Nat. Nanotech.*, vol. 5, p. 190, 2010.

[11] M. Wang, L. Fu, L. Gan, C. Zhang, M. Rümmeli, A. Bachmatiuk, K. Huang, Y. Fang, Z. Liu, "CVD Growth of Large Area Smooth-edged Graphene Nanomesh by Nanosphere Lithography," *Sci. Rep.*, vol. 3, p. 1238, 2013.

[12] A. Sinitskii, J. M. Tour, "Patterning Graphene through the Self-Assembled Templates: Toward Periodic Two-Dimensional Graphene Nanostructures with Semiconductor Properties," *J. Am. Chem. Soc.* vol. 132, p. 14730, 2010.

[13] X. Liang, Y.-S. Jung, S. Wu, A. Ismach, D. L. Olynick, S. Cabrini, J. Bokor, "Formation of Bandgap and Subbands in Graphene Nanomeshes with Sub-10 nm Ribbon Width Fabricated via Nanoimprint Lithography," *Nano Lett.*, vol. 10, p. 2454, 2010.

[14] Z. J. Qi, J. A. Rodríguez-Manzo, A. R. Botello-Méndez, S. J. Hong, E. A. Stach, Y. W. Park, J.-C. Charlier, M. Drndić, A. T. C. Johnson, "Correlating Atomic Structure and Transport in Suspended Graphene Nanoribbons," *Nano Lett.*, vol. 14, p. 4238, 2014.

[15] J. A. Fürst, J. G. Pedersen, C. Flindt, N. A. Mortensen, M. Brandbyge, T. G. Pedersen, A.-P. Jauho, "Electronic properties of graphene antidot lattices," *New J. Phys.*, vol. 11, p. 095020, 2009.

[16] T. G. Pedersen, C. Flindt, J. Pedersen, N. A. Mortensen, A.-P. Jauho, K. Pedersen, "Graphene Antidot Lattices: Designed Defects and Spin Qubits," *Phys. Rev. Lett.*, vol. 100, p. 136804, 2008.

[17] R. Petersen, T. G. Pedersen, A.-P. Jauho, "Clar Sextet Analysis of Triangular, Rectangular, and Honeycomb Graphene Antidot Lattices," *ACS Nano*, vol. 5, p. 523, 2011.

[18] S. J. Brun, M. R. Thomsen, T. G. Pedersen, "Electronic and optical properties of graphene antidot lattices: comparison of Dirac and tight-binding models," *J. Phys.: Condens. Matter*, vol. 26, p. 265301, 2014.

[19] F. Ouyang, Z. Yang, S. Peng, X. Zheng, X. Xiong, "Antidot-dependent bandgap and Clar sextets in graphene antidot lattices," *Physica E*, vol. 56, p. 222, 2014.

[20] F. Ouyang, S. Peng, Z. Yang, Y. Chen, H. Zou, X. Xiong, "Bandgap opening/closing of graphene antidot lattices with zigzag-edged hexagonal holes," *Phys. Chem. Chem. Phys.*, vol. 16, p. 20524, 2014.

[21] D. Logoteta, P. Marconcini, C. Bonati, M. Fagotti, M. Macucci, "High-performance solution of the transport problem in a graphene armchair structure with a generic potential," *Phys. Rev. E*, vol. 89, p. 063309, 2014.

[22] E. D. Herbschleb, R. K. Puddy, P. Marconcini, J. P. Griffiths, G. A. C. Jones, M. Macucci, C. G. Smith, M. R. Connolly, "Direct imaging of coherent quantum transport in graphene p-n-p junctions," *Phys. Rev. B*, vol. 92, p. 125414, 2015.

[23] P. Marconcini, M. Macucci, "Symmetry-dependent transport behavior of graphene double dots," *J. Appl. Phys.*, vol. 114, p. 163708, 2013.

[24] M. R. Thomsen, S. J. Brun, T. G. Pedersen, "Dirac model of electronic transport in graphene antidot barriers," *J. Phys.: Condens. Matter*, vol. 26, p. 335301, 2014.

[25] J. Tworzydło, B. Trauzettel, M. Titov, A. Rycerz, C. W. J. Beenakker, "Sub-Poissonian Shot Noise in Graphene," *Phys. Rev. Lett.*, vol. 96, p. 246802, 2006.

[26] M. V. Berry, R. J. Mondragon, "Neutrino billiards: time-reversal symmetry-breaking without magnetic fields," *Proc. R. Soc. Lond. A*, vol. 412, p. 53, 1987.

[27] E. McCann, V. I. Fal'ko, "Symmetry of boundary conditions of the Dirac equation for electrons in carbon nanotubes," *J. Phys.: Condens. Matter*, vol. 16, p. 2371, 2004.

[28] L. Brey, H. A. Fertig, "Electronic states of graphene nanoribbons studied with the Dirac equation," *Phys. Rev. B*, vol. 73, p. 235411, 2006.

[29] P. Marconcini, D. Logoteta, M. Macucci, "Sinc-based method for an efficient solution in the direct space of quantum wave equations with periodic boundary conditions," *J. Appl. Phys.*, vol. 114, p. 173707, 2013.

[30] S. Datta, *Electronic Transport in Mesoscopic Systems*, Cambridge, UK: Cambridge University Press, 1997.

[31] M. Büttiker, Y. Imry, R. Landauer, S. Pinhas, "Generalized many-channel conductance formula with application to small rings," *Phys. Rev. B*, vol. 31, p. 6207, 1985.

[32] M. Büttiker, "Scattering theory of thermal and excess noise in open conductors," *Phys. Rev. Lett.*, vol. 65, p. 2901, 1990.

[33] P. W. Anderson, "Absence of Diffusion in Certain Random Lattices," *Phys. Rev.*, vol. 109, p. 1492, 1958.

[34] Z. Fan, A. Uppstu, A. Harju, "Electronic and transport properties in geometrically disordered graphene antidot lattices," *Phys. Rev. B*, vol. 91, p. 125434, 2015.

Paolo Marconcini Paolo Marconcini (M'13) received the master's (summa cum laude) degree in Electrical Engineering and the Ph.D. degree in Electrical and Computer Engineering from the Università di Pisa, Pisa, Italy, in 2002 and 2006, respectively. Since 2006, he has been a Post-Doctoral Researcher with the Università di Pisa, where he is currently a Tenure-Track Researcher. In 2015 he received the Italian National Scientific Qualification for Associate Professor in Electronics. He has authored over 90 papers in international journals and proceedings. His current research interests include the study of nanoelectronic devices based on semiconductor heterostructures, nanowires, carbon nanotubes, and graphene, and of electronic systems for railway applications.

Massimo Macucci Massimo Macucci received the Degree in Electrical Engineering from the Università di Pisa, Pisa, Italy, in 1987, the Perfezionamento degree from the Sant'Anna School of Advanced Studies, Pisa, in 1990, and the Master's and Ph.D. degrees from the University of Illinois at UrbanaChampaign, Champaign, IL, USA, in 1991 and 1993, respectively. He has been a Faculty Member with the Electrical and Computer Engineering Department, Università di Pisa, since 1992, where he is currently a Professor of Electronics. He has authored over 150 peer-reviewed publications. His current research interests include novel nanoelectronic semiconductor devices, quantum effects in electron devices, noise phenomena in electronic components and circuits, and electronics for transportation applications.